Analyst

Accepted Manuscript

ROYAL SOCIETY OF CHEMISTRY

www.rsc.org/analyst

Combined use of quantitative ED-EPMA, Raman microspectrometry, and ATR-FTIR imaging techniques for the analysis of individual particles

Hae-Jin Jung[1,+], Hyo-Jin Eom[1,+], Hyun-Woo Kang[1], Myriam Moreau[2], Sophie Sobanska[2], and Chul-Un Ro[1,*]

[1] Department of Chemistry, Inha University, Yonghyun Dong, Nam Gu, 402-751, Incheon, South Korea

[2] Laboratoire de Spectrochimie Infrarouge et Raman, UMR CNRS 8516, Université de Lille 1, Bât. C5, 59655 Villeneuve d'Ascq Cedex, France

ABSTRACT

In this work, quantitative energy-dispersive electron probe X-ray microanalysis (ED-EPMA) (called low-*Z* particle EPMA), Raman microspectrometry (RMS), and attenuated total reflectance Fourier transform infrared spectroscopic (ATR-FTIR) imaging were applied in combination for the analysis of the same individual airborne particles for the first time. After examining individual particles of micrometer size by low-*Z* particle EPMA, consecutive examinations by RMS and ATR-FTIR imaging of the same individual particles were then performed. The relocation of the same particles on Al or Ag foils was successfully carried out among the three standalone instruments for several standard and an indoor airborne particle samples, resulting in the successful acquisition of quality spectral data from the three single-particle analytical techniques. The combined application of the three techniques to several different standard particles confirmed that those techniques provided consistent and complementary chemical composition information on the same individual particles. Further, it was clearly demonstrated that the three different types of spectral and imaging data from the same individual particles in an indoor aerosol sample provided richer information on physicochemical characteristics of the particle ensemble than that obtainable by the combined use of two single-particle analytical techniques.

Keywords: Single particle analysis, low-*Z* particle EPMA, Raman microspectrometry, ATR-FTIR imaging, atmospheric aerosols

+ Authors with equal contributions
* Corresponding author. Tel: +82 32 860 7676; fax: +82 32 867 5604; E-mail address: curo@inha.ac.kr

1. Introduction

As atmospheric particles are chemically and morphologically heterogeneous, and the average composition and average aerodynamic diameter obtained by the traditional bulk analyses do not describe well the population of the particles, micro-analytical single particle analyses have proven to be useful for studying atmospheric particles. Over the last 40 years, some advanced micro-beam analytical techniques have been used to provide spatially resolved information on the physical, morphological, and chemical properties of single particles formed in the atmosphere or in the laboratory.[1-5] Among them, energy-dispersive electron probe X-ray microanalysis (ED-EPMA) based on a scanning electron microscope (SEM) equipped with an ultrathin energy-dispersive X-ray (EDX) detector, provides information on the size and elemental compositions of individual particles with submicron lateral resolution.[1,4] Computer-controlled SEM/EDX can provide quantitative information on the elemental composition of a large number of particles[6-9], and has been used successfully to characterize a range of atmospheric aerosol samples.[10-19] Although very powerful, ED-EPMA has limited capabilities for performing molecular speciation of particles and probing semivolatile particles under non-destructive conditions due to the electron beam used and/or high vacuum maintained in the sample chamber. Alternatively, vibrational spectroscopic techniques are powerful for functional group analysis and molecular speciation of organic and inorganic chemical compounds including hydrated species under ambient conditions. Thus far, studies of the molecular characterization and/or hygroscopic properties of size-segregated aerosol particle samples have often been performed using confocal Raman microspectrometry (RMS)[20-22] or Fourier transform infrared (FTIR) spectroscopy[23-29].

Recently, the combined application of ED-EPMA and vibrational microspectrometric techniques for the characterization of heterogeneous individual particle ensembles was reported.[30-43] In particular, the combination of RMS and ED-EPMA has been applied for a decade because it can provide unambiguous chemical and structural information on heterogeneous environmental particles with a spatial resolution of <1 μm^2.[30,31,35,37,40-43] As ED-EPMA provides information on the morphology and elemental concentrations and RMS gives information on the molecular species and chemical mixing states, it would be much useful if ED-EPMA and RMS data would be obtained for the same individual particles. However, in most of previous studies, only Raman point analysis was performed without the systematic elemental quantification obtainable by ED-EPMA, and/or RMS and ED-EPMA were applied separately for aerosol samples (not on the same individual particles), mainly due

to the difficulty in the relocation of the same individual particles. In order to correctly relocate individual particles and acquire ED-EPMA and Raman data from the same spot without sample transfer, a dedicated instrument, called Structural and Chemical Analyzer (SCA) (a combined SEM and Raman spectrometer), was developed although its first application for the characterization of soil and lichen samples just appeared recently.[44] However, the practical problems of fine particle relocation, laser beam damage, and low Raman sensitivity encountered in SCA measurements, as well described elsewhere[43], still make this approach for obtaining quality ED-EPMA and Raman data from the same individual airborne particles of (sub)micrometer size a challenge. Another approach to obtain both ED-EPMA and Raman data from the same individual particles is to use standalone SEM/EDX and RMS instruments in parallel. Quite recently, two successful works were reported for the characterization of the same individual airborne particles using both quantitative ED-EPMA, called low-*Z* particle EPMA, and Raman imaging.[32,45] Also, the potential of the combined use of low-*Z* particle EPMA and attenuated total reflectance FTIR (ATR-FTIR) imaging for the characterization of the same individual aerosol particles (but at different spatial resolutions) has been recently reported.[33,34,36,38,39] FTIR imaging technique can provide information on the spatial distribution of chemical constituents within a sample, which can be used to characterize aerosol particles on a single particle basis. In particular, ATR-FTIR imaging can provide a spatial resolution of 3.1 μm at 1726 cm^{-1} [46,47], which is feasible for the single-particle characterization of airborne particles when used with low-*Z* particle EPMA in combination.

Although RMS and ATR-FTIR are similar in that they belong to vibrational spectroscopic techniques, their vibrational signals are generated from different fundamentals; i.e. RMS provides information on molecular vibrations based on the difference in wavelength between the incident and scattered visible radiation (Raman scattering), whereas ATR-FTIR based on the attenuation of the evanescent wave generated by the total reflected mid-IR radiation on the IRE crystal. According to selection rules, for IR spectroscopy it is necessary for the molecule to have a permanent electric dipole and for Raman spectroscopy it is the polarizability of the molecule which is important. Therefore, the differences in their spectra owing to their different signal generation mechanisms (i.e. scattering vs absorption of energy) and different selection rules would make two fingerprint techniques rather complementary. RMS and ATR-FTIR imaging provide spectra with a typical spectral range between 100 and 4000 cm^{-1} and 680-4000 cm^{-1}, respectively, making RMS efficient to identify metal oxides in

particle samples for example. Further, due to the incident radiation, RMS has better lateral resolution than ATR-FTIR imaging has, so that RMS is more powerful for the investigation of mixing state of individual particles. Although both RMS and ATR-FTIR have comparable axial resolutions (0.5-5 μm) depending on the sample properties, RMS can possibly provide depth imaging even on single particles as it can work in confocal measurement set-up. RMS and ATR-FTIR measurements can be done in ambient condition without sample preparation or modification. Raman spectra can reflect the real nature of individual particles more, and their mostly sharp Raman peaks are very useful for the unambiguous molecular speciation even for water-containing samples because H_2O molecules exhibit strong absorption in FTIR which may overlap the other IR bands. On the other hand, laser beam employed in RMS can induce damage on individual particles and the interference by the fluorescence often encountered in RMS needs to be minimized, which are not the problem in ATR-FTIR measurements. Finally, ATR-FTIR imaging provides ATR-FTIR spectrum at each pixel in image field, which is valuable for obtaining information on the molecular species for all individual particles sitting on the image field within several hours, whereas RMS mapping to obtain the spatial, chemical heterogeneity for individual particles takes much longer time as RMS images are acquired by point-by-point scanning mode.

Previous studies showed that the characterization of individual particles including chemical speciation and mixing state analysis could be performed more in detail using low-*Z* particle EPMA and either RMS or ATR-FTIR imaging in combination than by using each single-particle technique alone.[32-34,36,38,39,44,45] As RMS and FTIR are also two complementary vibrational spectroscopic techniques, it would be more powerful for the characterization of heterogeneous airborne particle ensembles if spectral data by three single-particle analytical techniques, such as low-*Z* particle EPMA, RMS, and ATR-FTIR imaging, could be obtained for the same individual particles. This study demonstrates the potential of the combined use of quality low-*Z* particle EPMA, RMS, and ATR-FTIR imaging data for the characterization of the same individual particles of heterogeneous airborne particle ensemble. The relocation of the same individual particles on Al or Ag foils was successfully carried out among the three standalone instruments for several standard and an indoor airborne particle samples, resulting in the successful acquisition of quality spectral data from the three techniques. In this work, for the first time the combined use of three different types of spectral and imaging data from the same individual particles provides richer information on physicochemical characteristics of the particle ensemble than that obtainable by the combined use of two single-particle analytical techniques.

2. Experiment

2.1. Samples

Several different standard powder particles, such as calcite ($CaCO_3$, 99.99% from Aldrich), anhydrite ($CaSO_4$, 99.99% from Aldrich), gypsum ($CaSO_4 \cdot 2H_2O$, 98% from Aldrich), quartz (SiO_2, 99.99% from Aldrich), sodium sulfate (Na_2SO_4, 99.99% from Aldrich), sodium nitrate ($NaNO_3$, 99.999% from Aldrich), and K-feldspar (microcline, $KAlSi_3O_8$, NIST SRM70a), were used to examine X-ray, Raman, and ATR-FTIR spectral and imaging data analysis for the same individual standard particles. The standard particles of micrometer size (0.5-18 μm) were collected either on Ag or Al foil after grinding standard powders and screening ground dry particles with a 20 μm sieve. The metallic foils were simply rubbed over the surface of the ground particles and some particles adhering to the foils were analyzed. An indoor aerosol sample was investigated for physicochemical characteristics of the heterogeneous atmospheric particle ensemble through the combined use of low-*Z* particle EPMA, RMS, and ATR-FTIR imaging. The sample was collected at an underground shopping area nearby a subway station in Seoul, Korea. The underground sampling site was surrounded by shops selling garments, footwear, leather goods, cosmetics, snacks, and fast foods. Sampling was done on stage 2 (size range in aerodynamic diameter = 2.5-10 μm) of a 3-stage cascade impactor (Dekati PM-10 sampler) on January 11 in 2007 with sampling duration of 10 min to avoid collection of agglomerated particles. The particle sample collected on Al foil was put in plastic carriers, sealed, and stored in desiccators before EPMA, RMS, and ATR-FTIR imaging measurements. More details on the sample can be found elsewhere.[48]

2.2. Low-Z particle EPMA measurements

Low-*Z* particle EPMA measurements were carried out using a Jeol JSM-6390 SEM equipped with an Oxford Link SATW ultrathin window EDX detector allowing the detection of low-*Z* elements such as C, N, and O. The spectral resolution of the detector was 133 eV for Mn–Kα X-rays. The X-ray spectra were recorded using Oxford INCA Energy software. An accelerating voltage of 10 kV, beam current of 1.0 nA, and a typical measuring time of 15 s for each particle were used to ensure a low background level for the spectra, good sensitivity for low-*Z* element analysis, and statistically significant characteristic X-ray counts. EDX data acquisition for the individual particles was carried out manually in point analysis mode,

whereby the electron beam was focused on the center of each particle and X-rays were acquired while the beam remained fixed on this single spot. The net X-ray intensities for the chemical elements were obtained by a non-linear, least-square fitting of the collected spectra using the AXIL program.[49] The elemental concentrations of the individual particles were determined from their X-ray intensities using a Monte Carlo calculation combined with reverse successive approximations.[8] The quantitative procedure based on a Monte Carlo simulation combined with successive approximations provided accurate results to within a 12% relative deviation between the calculated and nominal elemental concentrations for the various standard particles.[8,50] Using the "expert system" program[9], the individual particles were classified into different particle types based on their chemical compositions and morphologies. The basic classification rules are reported elsewhere.[50]

2.3. RMS measurements

The particles collected either on Al or Ag foil were placed on the microscope stage of a confocal Raman microspectrometer (LabRAM HR, Horiba-Scientific) equipped with a 100×, 0.9 numerical aperture objective (Olympus). Raman scattering was performed at a wavelength of 632.8 nm using a He–Ne laser and detected with a N_2 cooled charge-coupled device (CCD) detector. The laser power delivered to the sample was approximately 8 mW, which could be attenuated by a set of neutral density filters with an optical density ranging from 2 to 10000. The spot size of the laser at the sample was estimated to be ~1 μm^2. The spectra and images were acquired using Labspec5 software. For each analysis, two spectral ranges, i.e., 100-1250 cm^{-1} and 1000-2000 cm^{-1}, were explored. The XYZ computer-controlled Raman mapping was performed by obtaining the Raman spectra in a point-by-point XY scanning mode with a 1 μm step and a 10 s integration time per pixel. Raman mapping generates a three dimensional data set ($x \times y \times \lambda$), i.e. $x \times y$ spectra, each containing $\lambda = 2040$ spectral elements corresponding to a spectral range of approximately 1000 cm^{-1} with a spectral resolution of 4 cm^{-1}. From this data set, the pure Raman spectrum and spatial distribution of each species was obtained with a powerful multivariate data treatment (SIMPLISMAX).[30,51]

2.4. ATR-FTIR imaging measurements

ATR-FTIR imaging measurements were performed using a Perkin Elmer Spectrum 100 FTIR spectrometer interfaced to a Spectrum Spotlight 400 FTIR microscope. An ATR accessory using a germanium hemispherical IRE crystal with a diameter of 600 μm was used

for ATR imaging. The ATR accessory was mounted on the X-Y stage of the FTIR microscope and the IRE crystal made contact with the sample through a force lever. The ultimate spatial resolution of IR imaging is approximately equal to the wavelength of the incident IR radiation. On the other hand, the hemispherical IRE crystal acts like a lens in that the IR beam is condensed when the beam strikes the IRE. The extent of condensation is proportional to the refractive index of the IRE material (e.g. 4.0 for germanium). Therefore, a spatial resolution of 3.1 μm at 1726 cm^{-1} (5.79 μm) was achieved beyond the ultimate spatial resolution limit.[46,47] A 16 x 1 pixel mercury cadmium telluride (MCT) array detector was used to obtain FTIR images with a pixel size of 1.56 μm. For each pixel, an ATR-FTIR spectrum, ranging from 680 to 4000 cm^{-1} with a spectral resolution of 8 cm^{-1}, was obtained from eight interferograms, which were co-added and Fourier-transformed. The position of the crystal on the sample was determined by optical microscopy equipped with a light-emitting diode and CCD camera. Optical imaging was used to identify the same single particles that were analyzed using low-*Z* particle EPMA or RMS before ATR-FTIR imaging. Spectral data processing was performed using Perkin Elmer Spectrum IMAGE software.

2.5. Combined use of low-Z particle EPMA, RMS, and ATR-FTIR imaging

The combined use of the three single-particle analytical techniques for an examination of the same individual standard particles was carried out off-line, i.e. low-*Z* particle EPMA measurements were first performed to obtain the morphological and elemental compositional information on individual particles. Raman measurements of the individual particles on the same image fields examined previously by low-*Z* particle EPMA were carried out after relocating the particles using SEIs from SEM and optical images available from RMS. The relocation of individual particles of (sub)micrometer size either on Al or Ag foil is somewhat tricky and sometimes time-consuming. Nonetheless, many SEIs obtained at various magnifications (30x - 1000x) at overall and specific areas of the Al or Ag foil were utilized to find out the same image field by visually examining the location pattern of particles on optical image fields provided by RMS and ATR-FTIR imaging instruments. Finally, ATR-FTIR imaging measurements were performed on the same individual particles, which were examined by low-*Z* particle EPMA and RMS after relocating the particles using the SEIs and optical images. ATR-FTIR imaging measurements were carried out last because standard particles were physically modified when the IRE crystal made contact with the sample for the ATR-FTIR imaging measurements. On the other hand, for the investigation of the indoor

airborne sample, low-*Z* particle EPMA was performed first, followed in order by ATR-FTIR imaging and RMS. When the RMS measurements were performed before ATR-FTIR imaging, textile particles in the sample were damaged by the laser beam in RMS, producing insufficient ATR-FTIR spectra for the chemical speciation. When low-*Z* particle EPMA, RMS, and ATR-FTIR imaging are applied in combination for the characterization of the same individual particles, the possible damage induced by electrons and/or laser beam for beam-sensitive particles needs to be carefully considered.

3. Results and discussion

3.1. Combined use of low-Z particle EPMA, RMS, and ATR-FTIR imaging for standard particles

In this study, the X-ray, Raman, and ATR-FTIR spectral and imaging data of the same micrometer-sized particles were obtained successfully for the first time. As a typical example, Fig. 1(A)-(D) shows an SEI obtained before the Raman measurement, a visible light optical image obtained from the Raman instrument, an ATR-FTIR principal component analysis (PCA) image, and an SEI obtained after the ATR-FTIR measurement, respectively, of the same 20 standard anhydrite particles sitting on Ag foil. Although the qualities of the SEIs, optical image, and ATR-FTIR image differ due to the inherently different spatial resolutions of the images, the same patterns of the particle location among the images ensured that the same micrometer-sized particles were observed. First, the X-ray spectral and imaging data of all the 20 particles in the image field were obtained by SEM/EDX. Second, the sample, ~ 1 x 1 cm^2 in size, was moved into a Raman spectrometer where an optical microscope was used to relocate the same particles examined by SEM/EDX. Subsequently, the Raman mapping data for all the individual particles on the image field was obtained. The sample was transferred off-line again to a standalone ATR-FTIR imaging instrument, where the same image field was relocated by using an optical microscope (image is not shown here). The ATR-FTIR imaging measurements were performed on the image field of ~ 150 x 120 μm^2 size, where the pixel number of the image was ~ 7400 considering the pixel size of 1.56 x 1.56 μm^2 for the ATR-FTIR image. All pixels in the image contain the full IR spectra, ranging from 680 to 4000 cm^{-1}. After the ATR-FTIR measurements, the sample was transferred off-line to SEM and an SEI of the same image field was obtained to determine how the contact between the IRE crystal and the sample was made.

The images and spectral data for the other standard particles, such as gypsum, calcite, quartz, sodium sulfate, sodium nitrate, and K-feldspar, were obtained by SEM/EDX, RMS, and ATR-FTIR imaging in the same way as for anhydrite, where the images and X-ray, Raman, and ATR-FTIR spectra provided the consistent chemical information from the same individual standard particles (see Electronic supplementary information (ESI)).

The images and spectra of two typical anhydrite and gypsum particles shown in Fig. 2 clearly indicate that the three single-particle analytical techniques provide consistent chemical and morphological information on the same individual particles. Fig. 2(A) shows the visible light optical and Raman mapping images and SEIs, where the different quality of the images is clearly seen. The intensity variations observed on the Raman images (Fig. 2(A2) and (A5)) is due to the variation of the focus point of the laser (i.e. on the surface or above the surface of the particle) depending on the surface topography of the particles. Anhydrite ($CaSO_4$) and gypsum ($CaSO_4 \cdot 2H_2O$) are calcium sulfates without and with crystal water, respectively. The different crystal structures between the anhydrite (orthorhombic) and gypsum (monoclinic) particles can be determined clearly from their different Raman and ATR-FTIR spectra (Fig. 2(C) and (D)), which closely match with the reported spectra (see Table S1 of ESI). Elemental compositional analysis by low-*Z* particle EPMA also provided a clue on the difference between the anhydrite and gypsum particles, i.e. the measured elemental concentrations are similar to the stoichiometry of anhydrite and gypsum (Ca: S: O = 1.0: 1.1: 4.0 and 1.0: 0.9: 5.5, respectively), even though the difference was not as clear as those by RMS and ATR-FTIR analyses. Similar combined analysis was performed for other standard particles and good agreement was observed between the elemental and molecular compositions (see Figs. S1-S11 in ESI).

In Fig. 1(C), which shows a PCA ATR-FTIR image obtained by the application of PCA after the first differentiation of the original ATR-FTIR spectra of all of pixels in the image, the particles were displayed in two different colors, i.e. green for anhydrite particles and white-pink for calcite. PCA analysis of the ATR-FTIR imaging data can produce their images in different colors for particles with different chemical compositions. Therefore, the PCA images are useful for examining the chemical heterogeneity of individual particles on the image field. Although the purity of the anhydrite standard particle sample was 99.99%, 3 out of the 20 particles in the image field, such as #4, 5, and 12 in Fig. 1 (and Fig. S12 in ESI), were calcite. The ATR-FTIR images obtained at the characteristic IR peaks for anhydrite and calcite, such as 1090 and 1400 cm^{-1}, respectively, clearly show the spatial distribution of each mineral, as shown in Fig. S12(B) of ESI. As shown in Fig. 1(A) and (B) and Fig. S12(A) of

ESI, particles #3 and #4 were spatially well segregated when low-*Z* particle EPMA and RMS measurements were performed, and the X-ray and Raman spectral data were obtained from the segregated particles. On the other hand, as shown in Fig. 1(C) and Fig. S12(B1) of ESI, particles #3 and #4 appear coagulated on the ATR-FTIR images. Indeed, the SEI obtained after the ATR-FTIR measurements (Fig. 1(D)) suggests that particles #3 and #4 agglomerated when the sample came in contact with the Ge IRE crystal. A large amount of FTIR image data can be obtained relatively quickly compared to RMS. Therefore, molecular screening of the particle samples can be performed easily with similar quality discrimination of chemical heterogeneity. The spatial heterogeneity of individual particles can be clearly determined using RMS. Fig. S12(A) of ESI shows the visible light optical image of the particles #3 and #4 obtained by optical microscopy in a Raman spectrometer (Fig. S12(A1)), together with their Raman images obtained after a Raman spectral data treatment using SIMPLISMAX (Fig. S12(A2)-(A4)), where anhydrite and calcite minerals are displayed in green and red colors, respectively. Raman analysis suggested that particle #3 is a pure anhydrite mineral and particle #4 is composed of anhydrite and calcite at its upper and lower parts, respectively (Fig. S12(A2)-(A4)). Another example of the good capability of RMS for an analysis of the internal mixing of different chemicals in single particles can be found for particle #9 of a standard gypsum sample (see Figs. S1 and S13 in ESI).

3.2. The combined use of low-Z particle EPMA, RMS, and ATR-FTIR imaging for the characterization of indoor aerosol particles

Fig. 3(A)-(D) shows an SEI obtained before the ATR-FTIR imaging measurements, a PCA ATR-FTIR image, a visible light optical image obtained from the Raman instrument after ATR-FTIR imaging, and an SEI obtained after the RMS measurement, respectively, of the same 51 airborne individual particles of the indoor aerosol sample. The same patterns of the particle location among the images ensured that the same micrometer-sized particles were observed. First, the morphological and X-ray spectral data of all 51 particles in the image field were obtained by SEM/EDX. Second, the sample, ~ 1 x 1 cm^2 in size, was moved to the ATR-FTIR imaging instrument, and the ATR-FTIR spectra for all the pixels on the same image field were obtained after relocating the same particles examined by SEM/EDX. ATR-FTIR imaging was performed on the image field, ~ 350 x 270 μm^2 in size. The sample was then transferred off-line again into a Raman spectrometer where the Raman mapping data for all the individual particles on the same image field was obtained after relocating the same

image field. After the RMS measurements, an SEI of the same image field was obtained by SEM to check what modification had occurred during the ATR-FTIR measurements due to IRE crystal contact with the sample and during the Raman measurements due to laser beam damage.

Fig. 4 shows SEI and optical image from SEM and Raman spectroscopy, respectively, of three exemplar particles encountered frequently in this indoor particle sample, together with their X-ray, Raman, and ATR-FTIR spectra. As shown in Fig. 4(A), particle #29 appeared peculiar and flat on its SEI and transparent on its optical image. Based on its X-ray spectral data, particle #29 is a type of organic particle containing C, N, and O with a small amount of S. Raman spectroscopy did not provide useful information on its molecular species because only a fluorescence signal, which is probably from some organic compounds, was observed. On the other hand, ATR-FTIR analysis clearly identified it as a textile particle, either azlon or silk, which was achieved by comparing its spectrum with that from a Perkin-Elmer FTIR spectra library.[36]

As shown in Fig. 4(B), particle #34 appears angular both on SEI and optical image, which is typical for mineral particles. X-ray analysis indicated that it is a SiO_2 mineral with minor carbonaceous species (atomic concentrations of Si, O, and C are 32.8%, 62.8%, and 3.6%, respectively). Airborne SiO_2 mineral particles can normally exist either as quartz or cristobalite, and RMS and ATR-FTIR analysis identified particle #34 as quartz based on their Raman band and IR peaks. Regarding the carbonaceous species present in its X-ray spectrum, the ATR-FTIR spectrum does not show any related peak, probably because it is IR-inactive elemental carbon. Indeed, the Raman spectrum of particle #34 showed strong Raman bands at 1354 and 1573 cm^{-1}, which are characteristic of elemental carbon, such as graphite and soot with a large Raman cross-section.[52] In addition, a fluorescence signal was present, indicating the presence of organic carbon (probably humic or humic-like substances in very small amounts that are not detectable by ATR-FTIR analysis). Ti was not detected by low-*Z* particle EPMA because its content was below the detection limit (<1 wt %), but a small amount of anatase (TiO_2) was detected by RMS based on its characteristic Raman bands.[53] The TiO_2 species was reported to be generally associated with swelling clay minerals[54], and mineral dust containing minor TiO_2 might act as an effective photocatalyst for atmospheric chemical reactions.[55,56] In particular, it was recently reported that TiO_2 is involved in the renoxification process.[57] The combined application of the three single particle analytical techniques indicates that particle #34 is a quartz particle mixed with a minor amount of

anatase and elemental carbon along with very minor amounts of organic carbon (notated as quartz/anatase/elemental carbon in Fig. 4(B)).

As shown in Fig. 4(C), particle #18 appears agglomerated with many nano-sized particles, which is typical for iron-containing underground subway particles generated mainly from mechanical wear and friction processes at the rail-wheel-brake interfaces.[32,58-60] X-ray analysis indicated that it is an iron oxide particle with minor carbonaceous species (atomic concentrations of Fe, O, and C are 37.0%, 58.3%, and 4.8%, respectively). Iron oxides can exist with three different forms, such as magnetite (Fe_3O_4), hematite (α-Fe_2O_3), and maghemite (γ-Fe_2O_3) with different magnetic properties[61] and toxicities[62,63]. On the other hand, X-ray analysis cannot provide clear chemical speciation of the iron oxides in particle #18. In addition, ATR-FTIR is blind to the analysis of iron oxides due to the absence of characteristic IR peaks in the 680-4000 cm^{-1} spectral range. RMS is helpful for detecting the presence of both hematite and magnetite based on the hematite Raman bands at 225, 291, 410, 496, and 610 cm^{-1} and a magnetite band at 658 cm^{-1}.[64,65] In addition, the carbonaceous species present in the X-ray spectrum is only elemental carbon, which was suggested by the presence of Raman bands at 1315 and 1590 cm^{-1}, no fluorescence in the Raman spectrum, and no peak in the ATR-FTIR spectrum. The combined application of the three single-particle analytical techniques indicates that particle #18 is a hematite and magnetite mixture with a small amount of elemental carbon (notated as hematite/magnetite/elemental carbon in Fig. 4(C)).

Table 1 lists the chemical speciation results by the use of the three data in combination for the 51 individual indoor particles. The chemical species that were assigned either by low-*Z* particle EPMA, ATR-FTIR imaging, or RMS analysis are given in the third-fifth columns of Table 1. The sixth column of Table 1 lists the chemical species determined by the combined use of the three single-particle analytical data. Among the overall 51 individual particles analyzed, five different major species were classified, i.e. 12 textile particles, 7 mineral particles on textile one, 14 silicate mineral particles, 3 $CaCO_3$-containing particles, 9 particles mixed with silicates and $CaCO_3$, and 6 iron-containing particles.

The chemical speciation of the 12 textile particles, which were found to be either azlon or silk, was clearly obtained by ATR-FTIR analysis, which is supported by morphological and elemental concentration data from low-*Z* particle EPMA analysis, whereas RMS showed that these textile particles are organic by revealing only strong fluorescent signals. In addition, 7 mineral particles were also found to be sitting on textile

particles. For these particles, the ATR-FTIR spectral data was useful in identifying their mineral types because the IR peaks of the textile particles could be differentiated from those of the minerals, which is supported by low-*Z* particle EPMA analysis (see Table 1).

Fourteen particles were assigned as silicates (Table 1). As there are many different types of silicates, low-*Z* particle EPMA cannot identify unambiguously the specific form of aluminosilicate minerals alone so that aluminosilicate particles are denoted as "AlSi" in the third column of Table 1. On the other hand, ATR-FTIR analysis is useful for the chemical speciation of individual silicate particles when used with low-*Z* particle EPMA in combination.[33,34,39] RMS provided information on the presence of organic or elemental carbons based on the fluorescence or elemental carbon Raman signals. As listed in Table 1, the specific mineral forms, including their carbonaceous species, of all the 14 silicate particles were identified by the combined use of the three techniques for these silicate particles.

The $CaCO_3$-containing particles are also abundant in this sample (three $CaCO_3$ particles and nine particles mixed with $CaCO_3$ and silicates; see Table 1). When silicates are mixed with $CaCO_3$, RMS shows fluorescence and/or elemental carbon, which are similarly observed for the silicate particles. The combined use of low-*Z* particle EPMA and ATR-FTIR analyses was found to be useful for the chemical speciation of these $CaCO_3$-containing particles, along with additional information from RMS on carbonaceous species.

As described for particle #18 above, ATR-FTIR cannot detect iron-containing particles. On the other hand, RMS is powerful because it covers the spectral range of 100-670 cm^{-1}, where the Raman bands of iron oxides are observed. The chemical species of iron oxides in the subway particles have been in dispute for a long-time because they are related to their different toxicities.[62,63] Subway particles collected in a subway station in Stockholm, Sweden, were found to be eight times more genotoxic than urban street particles because iron-containing subway particles were crudely claimed to be in the form of magnetite, which has adverse health effects. On the other hand, major iron oxide particles collected at a subway station in Budapest, Hungary, were reported to be comprised mostly of relatively harmless hematite with small amounts of magnetite.[58] A recent XRD study reported that hematite is the major particle type in particles collected at a subway station in Barcelona, Spain.[67] According to this study, the combined use of RMS and low-*Z* particle EPMA revealed that hematite and magnetite are mixed in individual iron-containing particles.

4. Conclusions

In this study, the potential of the combined use of three single-particle analytical techniques (low-*Z* particle EPMA, RMS, and ATR-FTIR imaging) for an analysis of the same individual particles was investigated. For standard mineral particles, the X-ray, Raman, and ATR-FTIR spectral data of the same individual particles provided information on their chemical species, which were consistent between them. Morphological and elemental concentration information was obtained from low-*Z* particle EPMA analysis. Information on the molecular species and internal mixing state could be obtained by RMS and ATR-FTIR imaging techniques, with RMS having better capability for chemical heterogeneity analysis.

When this analytical methodology was applied to an indoor sample, the morphology and elemental concentration data of 51 individual particles on an image field were obtained using SEM/EDX. Quality RMS and ATR-FTIR data were obtained for all the particles. However, some Raman spectra were obscured by strong fluorescence from organic species, which appear to be somewhat common in real airborne aerosol particles. Because RMS covers the far IR spectral range, the chemical speciation from the far IR spectral data is quite valuable for metal-containing compounds, such as iron oxide particles. On the other hand, the identification of iron metal was only feasible from low-*Z* particle EPMA because RMS and ATR-FTIR are blind to the detection of iron metal. ATR-FTIR analysis was useful for chemical speciation of mineral and textile particles. In this work, the application of the three single-particle analytical techniques for an analysis of the same individual airborne particles provided richer information on their physicochemical characteristics than when those techniques were used alone or when two techniques in combination. As ATR-FTIR imaging, RMS, and low-*Z* particle EPMA have their own advantages and disadvantages, future studies should examine the optimal analytical procedure for the combined use of the three techniques.

Acknowledgements

This study was supported by Basic Science Research Programs through the National Research Foundation of Korea (NRF) funded by the Ministry of Education, Science, and Technology (NRF-2011-0008172 and NRF-2012R1A2A1A05026329) and by a French-Korean joint research project funded by the NRF and CNRS (Programme Hubert Curien STAR N° 19040UJ and NRF- 2013K1A3A1A21000340). M. Moreau and S. Sobanska thank Labex CaPPA (ANR-11-LABX-0005-01) and IRENI programs for their financial supports.

Electronic supplementary information available

The supplementary online data can be found in a file named “Supplementary data.doc”..

References

[1] De Bock, L. A.; Van Grieken, R., in *Analytical Chemistry of Aerosols*, ed. K. R. Spurny. Lewis Publishers, Boca Raton, FL, 1999, pp 243-272.

[2] Fletcher, R. A.; Small, J. A.; Scott, J. H. J., in *Aerosol Measurement: Principles, Techniques, and Applications*, ed. P. A. Baron, K. Willeke. 2nd ed., Wiley-Interscience, New York, 2001, pp 295-363.

[3] Ghorai, S.; Tivanski, A. V. Hygroscopic behavior of individual submicrometer particles studied by X-ray spectromicroscopy. *Anal. Chem.* **2010**, *82*, 9289-9298.

[4] Laskin, A., in *Fundamental and Application in Aerosols Spectroscopy*, ed. R. Signorell, J. Reid. Taylor and Francis Books, Inc., Boca Raton, FL, 2010, pp 243-272.

[5] Moffet, R. C.; Henn, T.; Laskin, A.; Gilles, M. K. Automated chemical analysis of internally mixed aerosol particles using X-ray spectromicroscopy at the carbon K-edge. *Anal. Chem.* **2010**, *82*, 7906-7914.

[6] Choël, M.; Deboudt, K.; Osán, J.; Flament, P.; Van Grieken, R. Quantitative determination of low-Z elements in single atmospheric particles on Boron substrates by automated scanning electron microscopy−energy-dispersive X-ray spectrometry. *Anal. Chem.* **2005**, *77*, 5686-5692.

[7] Ro, C.-U.; Osán, J.; Van Grieken, R. Determination of low-Z elements in individual environmental particles using windowless EPMA. *Anal. Chem.* **1999**, *71*, 1521-1528.

[8] Ro, C.-U.; Osán, J.; Szalóki, I.; de Hoog, J.; Worobiec, A.; Van Grieken, R. A monte carlo program for quantitative electron-induced X-ray analysis of individual particles. *Anal. Chem.* **2003**, *75*, 851-859.

[9] Ro, C.-U.; Kim, H.; Van Grieken, R. An expert system for chemical speciation of individual particles using low-Z particle electron probe X-ray microanalysis data. *Anal. Chem.* **2004**, *76*, 1322-1327.

[10] Choël, M.; Deboudt, K.; Flament, P.; Aimoz, L.; Mériaux, X. Single-particle analysis of atmospheric aerosols at Cape Gris-Nez, English Channel: Influence of steel works on iron apportionment. *Atmos. Environ.* **2007**, *41*, 2820-2830.

[11] Choël, M.; Deboudt, K.; Flament, P. Development of time-resolved description of aerosol properties at the particle scale during an episode of industrial pollution plume. *Water Air Soil Pollut.* **2010**, *209*, 93-107.

[12] Ebert, M.; Weinbruch, S.; Hoffmann, P.; Ortner, H. M. The chemical composition and complex refractive index of rural and urban influenced aerosols determined by individual particle analysis. *Atmos. Environ.* **2004**, *38*, 6531-6545.

[13] Geng, H.; Park, Y.; Hwang, H.; Kang, S.; Ro, C.-U. Elevated nitrogen-containing particles observed in Asian dust aerosol samples collected at the marine boundary layer of the Bohai Sea and the Yellow Sea. *Atmos. Chem. Phys.* **2009**, *9*, 6933-6947.

[14] Geng, H.; Ryu, J.; Jung, H.-J.; Chung, H.; Ahn, K.-H.; Ro, C.-U. Single-particle characterization of summertime arctic aerosols collected at Ny-Alesund, Svalbard. *Environ. Sci. Technol.* **2010**, *44*, 2348-2353.

[15] Kang, S.; Hwang, H.; Park, Y.; Kim, H.; Ro, C.-U. Chemical compositions of subway particles in Seoul, Korea determined by a quantitative single particle analysis. *Environ. Sci. Technol.* **2008**, *42*, 9051-9057.

[16] Kang, S.; Hwang, H.; Park, Y.; Kim, H.; Ro, C.-U. Quantitative ED-EPMA combined with morphological information for the characterization of individual aerosol particles collected in Incheon, Korea. *Atmos. Environ.* **2009**, *43*, 3445-3453.

[17] Krueger, B. J.; Grassian, V. H.; Iedema, M. J.; Cowin, J. P.; Laskin, A. Probing heterogeneous chemistry of individual atmospheric particles using scanning electron microscopy and energy-dispersive X-ray analysis. *Anal. Chem.* **2003**, *75*, 5170-5179.

[18] Ro, C.-U.; Hwang, H.; Kim, H.; Chun, Y.; Van Grieken, R. Single-particle characterization of four "Asian Dust" samples collected in Korea, using low-Z particle electron probe X-ray microanalysis. *Environ. Sci. Technol.* **2005**, *39*, 1409-1419.

[19] Worobiec, A.; Szalóki, I.; Osán, J.; Maenhaut, W.; Stefaniak, E. A.; Van Grieken, R. Characterisation of Amazon Basin aerosols at the individual particle level by X-ray microanalytical techniques. *Atmos. Environ.* **2007**, *41*, 9217-9230.

[20] Chan, M. N.; Chan, C. K. Hygroscopic properties of two model humic-like substances and their mixtures with inorganics of atmospheric importance. *Environ. Sci. Technol.* **2003**, *37*, 5109-5115.

[21] Freedman, M. A.; Baustian, K. J.; Wise, M. E.; Tolbert, M. A. Characterizing the morphology of organic aerosols at ambient temperature and pressure. *Anal. Chem.* **2010**, *82*, 7965-7972.

[22] Treuel, L.; Sandmann, A.; Zellner, R. Spatial separation of individual substances in effloresced crystals of ternary ammonium sulphate/dicarboxylic acid/water aerosols. *Chem. Phys. Chem.* **2011**, *12*, 1109-1117.

[23] Bruns, E. A.; Perraud, V.; Zelenyuk, A.; Ezell, M. J.; Johnson, S. N.; Yu, Y.; Imre, D.; Finlayson-Pitts, B. J.; Alexander, M. L. Comparison of FTIR and particle mass spectrometry for the measurement of particulate organic nitrates. *Environ. Sci. Technol.* **2010**, *44*, 1056-1061.

[24] Coury, C.; Dillner, A. M. A method to quantify organic functional groups and inorganic compounds in ambient aerosols using attenuated total reflectance FTIR spectroscopy and multivariate chemometric techniques. *Atmos. Environ.* **2008**, *42*, 5923-5932.

[25] Garland, R. M.; Wise, M. E.; Beaver, M. R.; DeWitt, H. L.; Aiken, A. C.; Jimenez, J. L.; Tolbert, M. A. Impact of palmitic acid coating on the water uptake and loss of ammonium sulfate particles. *Atmos. Chem. Phys.* **2005**, *5*, 1951-1961.

[26] Gibson, E. R.; Hudson, P. K.; Grassian, V. H. Physicochemical properties of nitrate aerosols: Implications for the atmosphere. *J. Phys. Chem. A* **2006**, *110*, 11785-11799.

[27] Hoffman, R. C.; Laskin, A.; Finlayson-Pitts, B. J. Sodium nitrate particles: physical and chemical properties during hydration and dehydration, and implications for aged sea salt aerosols. *J. Aerosol Sci.* **2004**, *35*, 869-887.

[28] Hopey, J. A.; Fuller, K. A.; Krishnaswamy, V.; Bowdle, D.; Newchurch, M. Fourier transform infrared spectroscopy of size-segregated aerosol deposits on foil substrates. J. *Appl. Optics* **2008**, *47*, 2266-2274.

[29] Liu, Y.; Yang, Z.; Desyaterik, Y.; Gassman, P. L.; Wang, H.; Laskin, A. Hygroscopic behavior of substrate-deposited particles studied by micro-FT-IR spectroscopy and complementary methods of particle analysis. *Anal. Chem.* **2008**, *80*, 633-642.

[30] Batonneau, Y.; Brémard, C.; Gengembre, L.; Laureyns, J.; Le Maguer, A.; Le Maguer, D.; Perdrix, E.; Sobanska, S. Speciation of PM_{10} Sources of airborne nonferrous metals within the 3-km Zone of lead/zinc smelters. *Environ. Sci. Technol.* **2004**, *38*, 5281-5289.

[31] Batonneau, Y.; Sobanska, S.; Laureyns, J.; Brémard, C. Confocal microprobe Raman imaging of urban Tropospheric aerosol particles. *Environ. Sci. Technol.* **2006**, *40*, 1300-1306.

[32] Eom, H.; Jung, H.; Sobanska, S.; Chung, S.; Son, Y.; Kim, J.; Sunwoo, Y.; Ro, C.-U. Iron Speciation of Airborne Subway Particles by the Combined Use of Energy Dispersive Electron Probe X-ray Microanalysis and Raman Microspectrometry. *Anal. Chem*. **2013**, *85*, 10424–10431.

[33] Jung, H.-J.; Malek, M. A.; Ryu, J.; Kim, B.; Song, Y.-C.; Kim, H.; Ro, C.-U. Speciation of individual mineral particles of micrometer size by the combined use of attenuated total

reflectance-Fourier transform-infrared imaging and quantitative energy-dispersive electron probe X-ray microanalysis techniques. *Anal. Chem.* **2010**, *82*, 6193-6202.

[34] Malek, M. A.; Kim, B.; Jung, H.-J.; Song, Y.-C.; Ro, C.-U. Single-particle mineralogy of Chinese soil particles by the combined use of low-Z particle electron probe X-ray microanalysis and attenuated total reflectance-FT-IR imaging techniques. *Anal. Chem.* **2011**, *83*, 7970-7977.

[35] Nelson, M. P.; Zugates, C. T.; Treado, P. J.; Casuccio, G. S.; Exline, D. L.; Schlaegle, S. F. Combining Raman chemical imaging and scanning electron microscopy to characterize ambient fine particulate matter. *Aerosol Sci. Tech.* **2001**, *34*, 108-117.

[36] Ryu, J.; Ro, C.-U. Attenuated total reflectance FT-IR imaging and quantitative energy dispersive-electron probe X-ray microanalysis techniques for single particle analysis of atmospheric aerosol particles. *Anal. Chem.* **2009**, *81*, 6695-6707.

[37] Sobanska, S.; Falgayrac, G.; Laureyns, J.; Brémard, C. Chemistry at level of individual aerosol particle using multivariate curve resolution of confocal Raman image. *Spectrochim. Acta Part A* **2006**, *64*, 1102-1109.

[38] Song, Y.-C.; Ryu, J.; Malek, M. A.; Jung, H.-J.; Ro, C.-U. Chemical speciation of individual airborne particles by the combined use of quantitative energy-dispersive electron probe X-ray microanalysis and attenuated total reflection Fourier transform-infrared imaging techniques. *Anal. Chem.* **2010**, *82*, 7987-7998.

[39] Song, Y.-C.; Eom, H.-J.; Jung, H.-J.; Malek, M. A.; Kim, H. K.; Geng, H.; Ro, C.-U., Investigation of aged Asian dust particles by the combined use of quantitative ED-EPMA and ATR-FTIR imaging. *Atmos. Chem. Phys*. **2013**, *13*, 3463-3480.

[40] Stefaniak, E. A.; Worobiec, A.; Potgieter-Vermaak, S.; Alseczc, A.; Török, S.; Van Grieken, R. Molecular and elemental characterisation of mineral particles by means of parallel micro-Raman spectrometry and scanning electron microscopy/energy dispersive X-ray analysis. *Spectrochim. Acta Part B* **2006**, *61*, 824-830.

[41] Stefaniak, E.; Alseczc, A.; Frost, R.; Sajo, I.; Mathe, Z.; Török, S.; Worobiec, A.; Van Grieken, R. Combined SEM/EDX and micro-Raman spectroscopy analysis of uranium minerals from a former uranium mine. *J. Hazard. Mater.* **2009**, *168*, 416-423.

[42] Worobiec, A.; Stefaniak, E.; Potgieter-Vermaak, S.; Spolnik, Z.; Van Grieken, R. Characterisation of concentrates of heavy mineral sands by micro-Raman spectrometry and CC-SEM/EDX with HCA. *Appl. Geochem.* **2007**, *22*, 2078-2085.

[43] Worobiec, A.; Potgieter-Vermaak, S.; Brooker, A.; Darchuk, L.; Stefaniak, E.; Van Grieken, R. Interfaced SEM/EDX and micro-Raman Spectrometry for characterisation of

heterogeneous environmental particles - Fundamental and practical challenges. *Microchem. J.* **2010**, *94*, 65-72.

[44] Goienaga, N.; Sarmiento, A.; Olivares, M.; Carrero, J. A.; Fernandez, L. A.; Madariaga, J. M. Emerging application of a structural and chemical analyzer for the complete characterization of metal-rich particulate matter. *Anal. Chem*. **2013**, *85*, 7173-7181

[45] Sobanska, S.; Hwang, H.; Choël, M.; Jung, H.-J.; Eom, H.-J.; Kim, H.; Barbillat, J.; Ro, C.-U. Investigation of the chemical mixing state of individual Asian dust particles by the combined use of electron probe X-ray microanalysis and Raman microspectrometry. *Anal. Chem.* **2012**, *84*, 3145-3154.

[46] Van Dalen, G.; Heussen, P. C. M.; Den Adel, R.; Hoeve, R. B. J. Attenuated total internal reflection infrared microscopy of multilayer plastic packaging foils. *Appl. Spectrosc*. **2007**, *61*, 593-602.

[47] Crane, N. J.; Bartick, E. G.; Perlman, R. S.; Huffman, S. Infrared spectroscopic imaging for noninvasive detection of latent fingerprints. *J. Forensic Sci*. **2007**, *52*, 48-53.

[48] Maskey, S.; Kang, T.; Jung, H.-J.; Ro, C.-U. Single-particle characterization of indoor aerosol particles collected at an underground shopping area in Seoul, Korea. *Indoor Air* **2011**, *21*, 12-24.

[49] Vekemans, B.; Janssens, K.; Vincze, L.; Adams, F.; Van Espen, P. Analysis of X-ray spectra by iterative least squares (AXIL): New developments. *X-Ray Spectrom.* **1994**, *23*, 278-285.

[50] Ro, C.-U.; Oh, K.-Y.; Kim, H.; Kim, Y. P.; Lee, C. B.; Kim, K.-H.; Kang, C. H.; Osán, J.; de Hoog, J.; Worobiec, A.; Van Grieken, R. Single-particle analysis of aerosols at Cheju island, Korea, using low-Z electron probe X-ray microanalysis: A direct proof of nitrate formation from sea salts. *Environ. Sci. Technol.* **2001**, *35*, 4487-4494.

[51] Windig, W.; Antalek, B.; Lippert, J. L.; Batonneau, Y.; Brémard, C. Combined use of conventional and second-derivative data in the SIMPLISMA self-modeling mixture analysis approach. *Anal. Chem.* **2002**, *74*, 1371-1379.

[52] Sadezky, A.; Muckenhuber, H.; Grothe, H.; Niessner, R.; Pöschl, U. Raman microspectroscopy of soot and related carbonaceous materials: Spectral analysis and structural information. *Carbon* **2005**, *43*, 1731-1742.

[53] Choi, H.; Jung, Y.; Kim, S. Size effects in the Raman spectra of TiO_2 nanoparticles. *Vib. Spectrosc.* **2005**, *37*, 33-38.

[54] Allo, W. Authigenic Ti-bearing crystals in a Precambrian clay from Buenos Aires Province, Argentina. *Clays Clay Miner*. **2004**, *52*, 304−310.

[55] Monge, M. E.; D'Anna, B.; George, C. Nitrogen dioxide removal and nitrous acid formation on titanium oxide surfaces-an air quality remediation process? *Phys. Chem. Chem. Phys*. **2010**, *12*, 8991−8998.

[56] Ndour, M.; D'Anna, B.; George, C.; Ka, O.; Balkanski, Y.; Kleffmann, J.; Stemmler, K.; Ammann, M. Photoenhanced uptake of NO_2 on mineral dust: Laboratory experiments and model simulations. *Geophys. Res. Lett*. **2008**, *35*, L05812.

[57] Ndour, M.; Conchon, P.; D'Anna, B.; Ka, O.; George, C. Photochemistry of mineral dust surface as a potential atmospheric renoxification process. *Geophys. Res. Lett.* **2009**, *36*, L05816.

[58] Salma, I.; Pósfai, M.; Kovács, K.; Kuzmann, E.; Homonnay, Z.; Posta, J. Properties and sources of individual particles and some chemical species in the aerosol of a metropolitan underground railway station. *Atmos. Environ*. **2009**, *43*, 3460-3466.

[59] Jung, H.; Kim, B.; Ryu, Y.; Maskey, S.; Kim, J.-C.; Sohn, J.; Ro, C.-U. Source identification of particulate matter collected at underground subway stations in Seoul, Korea using quantitative single-particle analysis. *Atmos. Environ.* **2010**, *44*, 2287-2293.

[60] Jung, H.; Kim, B.; Malek, M.; Koo, Y; Jung, H.-J.; Son, Y.; Kim, J.-C.; Kim, H.; Ro, C.-U. Chemical speciation of size-segregated floor dusts and airborne magnetic particles collected at underground subway stations in Seoul, Korea. *J. Hazard. Mater*. **2012**, *213-214*, 331-340.

[61] Zhang, W.; Jiang, H.; Dong, C.; Yan, Q.; Yu, L.; Yu, Y. Magnetic and geochemical characterization of iron pollution in subway dusts in Shanghai, China. *Geochem. Geophy. Geosy*. **2011**, *12*, Q06Z25, doi:10.1029/2011GC003524.

[62] Karlsson, H. L.; Ljungman, A. G.; Lindbom, J.; Moller, L. Comparison of genotoxic and inflammatory effects of particles generated by wood combustion, a road simulator and collected from street and subway. *Toxicol. Lett*. **2006**, *165*, 203-211.

[63] Bachoual, R.; Boczkowski, J.; Goven, D.; Amara, N.; Tabet, L.; On, D.; Leçon-Malas, V.; Aubier, M.; Lanone, S. Biological effects of particles from the Paris subway system. *Chem. Res. Toxicol.* **2007**, *20*, 1426-1433.

[64] Faria, D.; Venâncio S.; Oliveira, M. Raman microspectroscopy of some iron oxides and oxyhydroxides. *J. Raman Spectrosc.* **1997**, *28*, 873-878.

[65] Legodi, M.; Waal, D. The preparation of magnetite, goethite, hematite and maghemite of pigment quality from mill scale iron waste. *Dyes Pigments* **2007**, *74*, 161-168.

[66] Karlsson, H. L.; Nilsson, L.; Möller, L. Subway particles are more genotoxic than street particles and induce oxidative stress in cultured human lung cells. *Chem. Res. Toxicol.* **2005**, *18*, 19-23.

[67] Querol, X.; Moreno, T.; Karanasiou, A.; Reche, C.; Alastuey, A.; Viana, M.; Font, O.; Gil, J.; De Miguel, E.; Capdevila, M. Variability of levels and composition of PM_{10} and $PM_{2.5}$ in the Barcelona metro system. *Atmos. Chem. Phys.* **2012**, *12*, 5055-5076.

Table 1. Chemical speciation either by low-Z particle EPMA, ATR-FTIR imaging, or RMS, and by the use of the three data in combination.

particle #	size (in μm)	chemical speciation by low-*Z* particle EPMA (minor elements)	chemical speciation by ATR-FTIR imaging	chemical speciation by RMS	chemical speciation by the combined use of three data
(A) Textile particles - azlon or silk					
3	16.3	C,N,O (Ca)	textile (azlon or silk)	no data	textile (azlon or silk)
4	9.9	C,N,O (S)	textile (azlon or silk)	fluorescence	textile (azlon or silk)
11	16.3	C,N,O (Na,S)	textile (azlon or silk)	fluorescence	textile (azlon or silk)
14	32.9	C,N,O (K)	textile (azlon or silk)	no data	textile (azlon or silk)
21	11.3	C,N,O (Ca,S)	textile (azlon or silk)	no data	textile (azlon or silk)
28	30.5	C,N,O (Na)	textile (azlon or silk)	no data	textile (azlon or silk)
29	21.4	C,N,O (S)	textile (azlon or silk)	fluorescence	textile (azlon or silk)
33	23.1	C,N,O (Na,S,K,Ca)	textile (azlon or silk)	fluorescence	textile (azlon or silk)
35	11.4	C,N,O (Na,Si,S,K,Ca)	textile (azlon or silk)	fluorescence	textile (azlon or silk)
38	20.3	C,N,O (S)	textile (azlon or silk)	no data	textile (azlon or silk)
42	17.0	C,N,O (Na,S)	textile (azlon or silk)	no data	textile (azlon or silk)
45	18.7	C,N,O (S)	textile (azlon or silk)	no data	textile (azlon or silk)
(B) Mineral particles on textile one					
12	5.9	C,N,O/AlSi/Na	textile/Na-feldspar	fluorescence	Na-feldspar/textile
22	4.0	C,O/AlSi/Ca(CO_3,SO_4)/C (Na,Mg,K,Fe)	textile/montmorillonite/ Ca(CO_3,SO_4)	fluorescence/ elemental carbon(EC)	montmorillonite/ Ca(CO_3,SO_4)/textile/EC
30	4.7	C,O/AlSi/$CaCO_3$/K	textile/K-feldspar/$CaCO_3$	fluorescence/EC	K-feldspar/ $CaCO_3$/textile/EC

31	8.9	C,N,O/AlSi/$CaCO_3$ (Na,Mg)	textile/motmorillonite/ $CaCO_3$	fluorescence	montmorillonite/ $CaCO_3$/textile
32	7.0	C,N,O/$CaCO_3$ (Si)	textile/$CaCO_3$/quartz	fluorescence	$CaCO_3$/quartz/textile
37	7.5	C,O/AlSi/Ca(CO_3,SO_4) (Na,Mg,Fe)	textile/montmorillonite/ Ca(CO_3,SO_4)	fluorescence/EC	montmorillonite/ Ca(CO_3,SO_4)/textile/EC
41	12.6	C,N,O/AlSi/Na,Ca	textile/(Na,Ca)-feldspar	fluorescence	(Na,Ca)-feldspar/textile
(C) Silicates					
1	4.1	AlSi/Na/C	Na-feldspar/organics	Na-feldspar/organics	Na-feldspar/organics
2	4.2	AlSi/K/C	K-feldspar	fluorescence/EC	K-feldspar/EC
6	3.2	AlSi/Na/C	Na-feldspar	fluorescence/EC	Na-feldspar/EC
7	2.8	SiO_2/C	crystobalite	fluorescence/EC	crystobalite/EC
10	4.3	AlSi/FeOx/Mg,C	Biotite	fluorescence/EC	biotite/FeOx/EC
17	4.3	AlSi/C (Na,Mg,Fe)	montmorillonite/organics	fluorescence/EC	montmorillonite/ organics/EC
20	3.6	SiO_2/C	quartz	fluorescence/EC	quartz/EC
24	6.3	SiO_2/C	crystobalite	fluorescence/EC	crystobalite/EC
25	4.2	AlSi/K/C (Mg,Fe)	muscovite/organics	fluorescence	muscovite/organics
27	2.7	AlSi/Na/C (Ca)	(Na,Ca)-feldspar/organics	fluorescence/EC	(Na,Ca)-feldspar/ organics
34	4.6	SiO_2/C	quartz	anatase/quartz/EC	quartz/anatase/EC
39	4.3	AlSi/Na/C	Na-feldspar/organics	fluorescence/EC	Na-feldspar/organics
47	4.3	AlSi/Na/C	Na-feldspar	fluorescence/EC	Na-feldspar/EC
51	5.4	AlSi/Na/C	Na-feldspar	fluorescence/EC	Na-feldspar/EC
(D) $CaCO_3$-containing particles					
16	4.6	$CaCO_3$	$CaCO_3$	$CaCO_3$	$CaCO_3$
19	4.2	C/$CaCO_3$	$CaCO_3$/amorphous calcium	fluorescence/EC	EC/$CaCO_3$/ACC

			carbonate(ACC)		
48	4.3	$CaCO_3$/C	$CaCO_3$/organics	$CaCO_3$	$CaCO_3$/organics
(E) Particles mixed with silicates and $CaCO_3$					
8	6.8	C/Ca(CO_3,SO_4)/AlSi (Na,Mg)	Ca(CO_3,SO_4)/ montmorillonite/organics	EC	EC/Ca(CO_3,SO_4)/ Montmorillonite/ organics
9	6.1	C/AlSi/$CaCO_3$ (Na,Mg,Fe)	montmorillonite/$CaCO_3$/ organics	fluorescence	montmorillonite/$CaCO_3$ /organics
13	6.5	C/Ca(CO_3,SO_4)/AlSi (Mg)	Ca(CO_3,SO_4)/ montmorillonite/organics	fluorescence	Ca(CO_3,SO_4)/ Montmorillonite/ organics
23	5.1	C/AlSi (Mg,K,Ca,Fe)	montmorillonite/$CaCO_3$/ organics	fluorescence/EC	montmorillonite/$CaCO_3$ /organics/EC
26	6.0	C/AlSi/$CaCO_3$/Na,K	(Na,K)-feldspar/ $CaCO_3$/organics	fluorescence	(Na,K)-feldspar/$CaCO_3$ /organics
36	8.5	C/AlSi/Ca(CO_3,SO_4) (Na,Mg)	montmorillonite/ Ca(CO_3,SO_4)/organics	fluorescence/EC	montmorillonite/ Ca(CO_3,SO_4)/organics/ EC
44	5.7	C/AlSi/Ca(CO_3,SO_4) (Na,Mg,Fe)	montmorillonite/ Ca(CO_3,SO_4)/organics	fluorescence/EC	montmorillonite/ Ca(CO_3,SO_4)/organics/ EC
46	8.1	AlSi/Ca(CO_3,SO_4)/C (Na,Mg,Fe)	montmorillonite/ Ca(CO_3,SO_4)	fluorescence/EC	montmorillonite/ Ca(CO_3,SO_4)/EC
49	4.5	AlSi/(Mg,Ca)CO3/Na/C	Na-feldspar/ (Mg,Ca)CO_3/organics	fluorescence/EC	Na-feldspar/ (Mg,Ca)CO_3/organics/ EC
(F) Fe-containing particles					
5	3.0	FeOx/Si,Ca,C	no IR peaks	hematite/magnetite/EC	hematite/magnetite/EC/ Si,Ca
15	7.2	FeOx/Si,Ca,C	no IR peaks	hematite/magnetite/EC	hematite/magnetite/EC/ Si,Ca
18	4.9	FeOx/C	no IR peaks	hematite/magnetite/EC	hematite/magnetite/EC

40	2.1	FeOx/Si,Ca,Cu,Ba,S,C	no IR peaks	hematite/magnetite/EC	hematite/magnetite/EC/ Si,Ca,Cu,Ba,S
43	5.1	FeOx/Si,Ca,C	no IR peaks	hematite/magnetite/EC	Hematite/magnetite/EC/ Si,Ca
50	3.6	FeOx/Si,Ca,C	no IR peaks	hematite/magnetite/EC	Hematite/magnetite/EC/ Si,Ca

Figure 1. (A) Secondary electron image (SEI) from SEM before ATR-FTIR measurement, (B) optical image from Raman spectrometer, (C) ATR-FT-IR image by PCA analysis, and (D) SEI after ATR-FTIR measurement of the same 20 anhydrite particles on Ag foil.

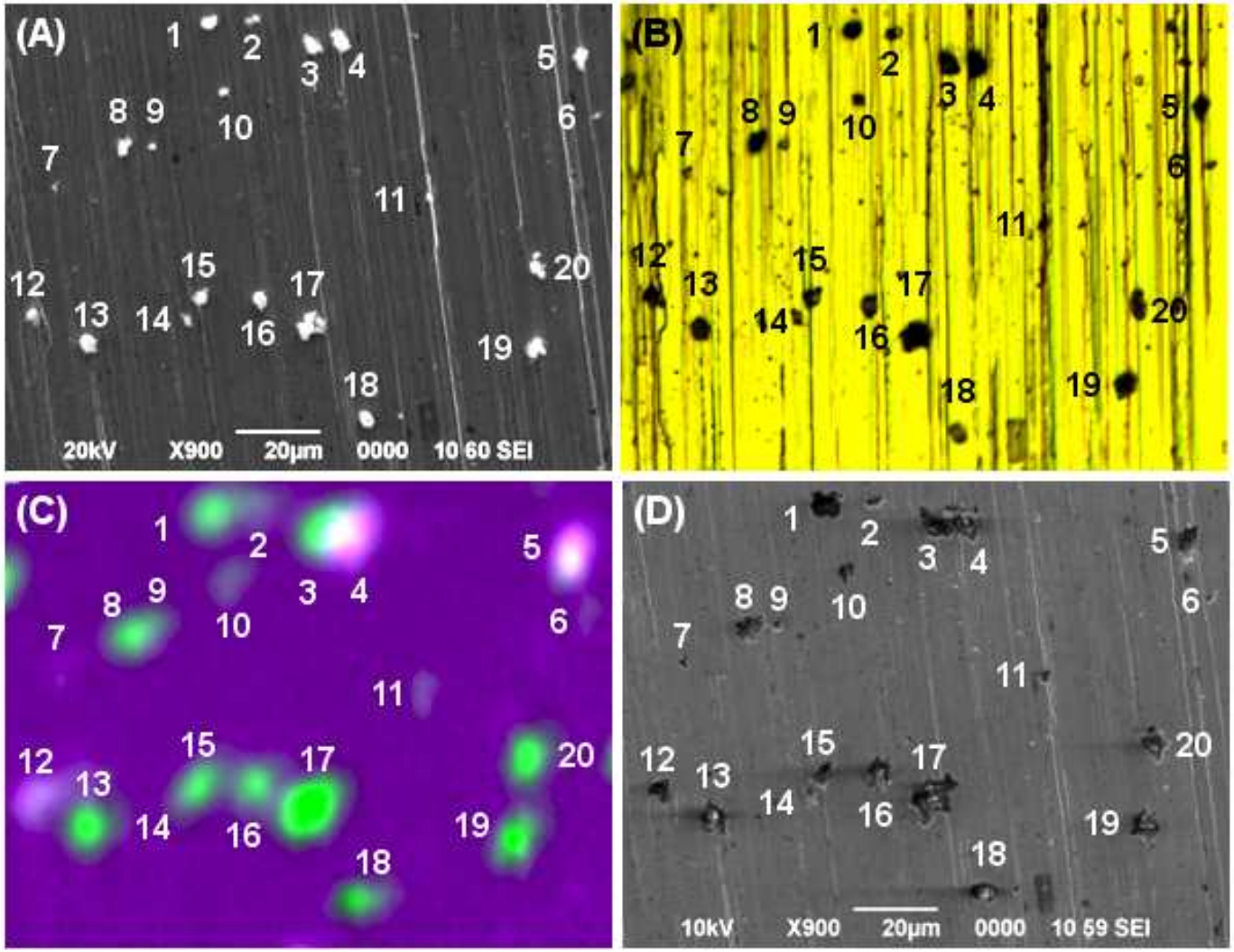

Figure 2. (A) Optical images from Raman spectrometer ((A1) and (A4)), corresponding Raman images ((A2) and (A5)), and SEIs ((A3) and (A6)) of the same anhydrite and gypsum particles, respectively, (B) their X-ray spectra, (C) Raman spectra, and (D) ATR-FT-IR spectra.

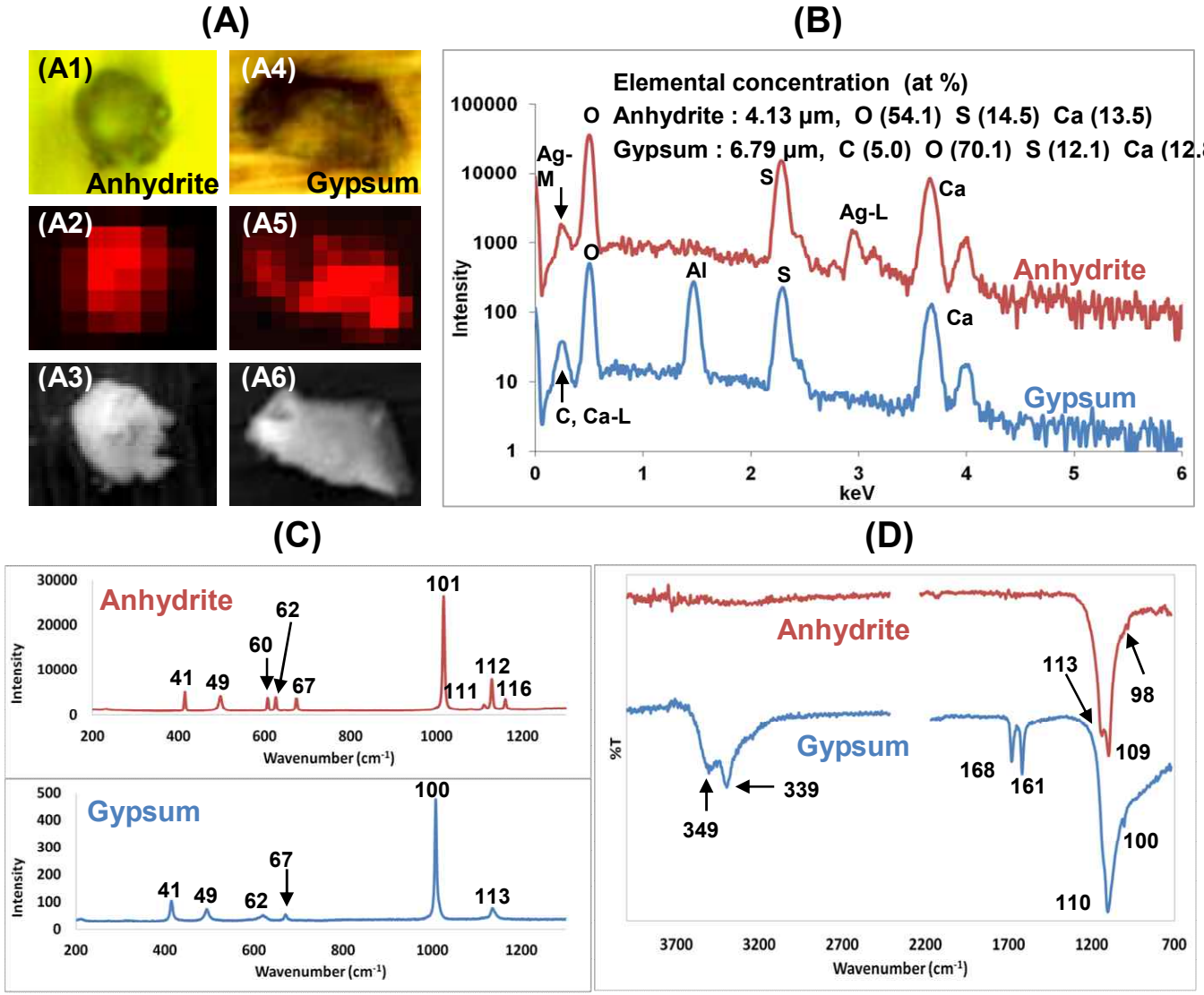

Figure 3. (A) Secondary electron image (SEI) from SEM before ATR-FTIR measurement, (B) ATR-FTIR PCA image, (C) optical image from Raman spectrometer, and (D) SEI after RMS measurement of the same 51 airborne indoor particles on Al foil.

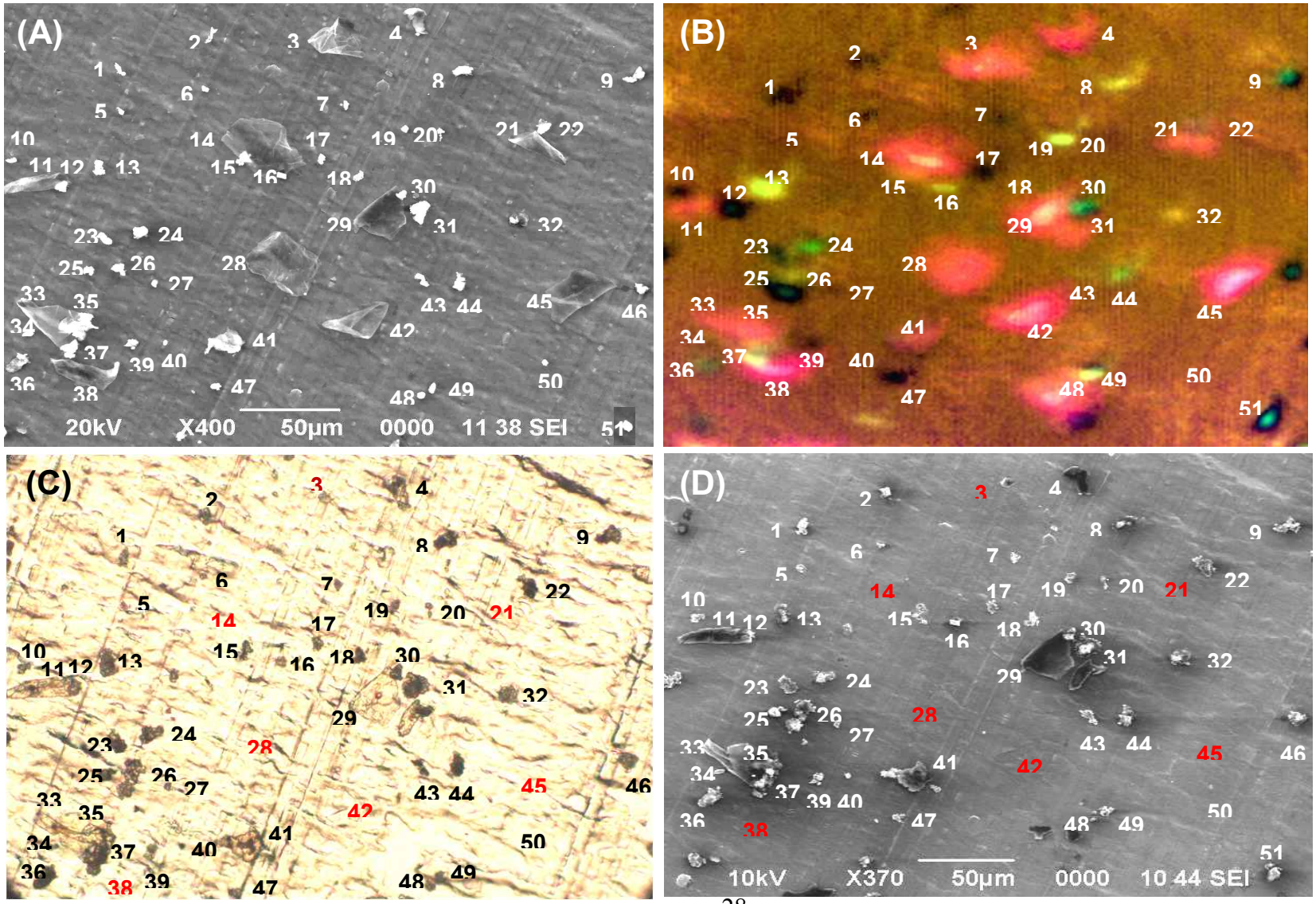

Figure 4. Three exemplar indoor particles with their morphological images and X-ray, Raman, and ATR-FTIR spectra.

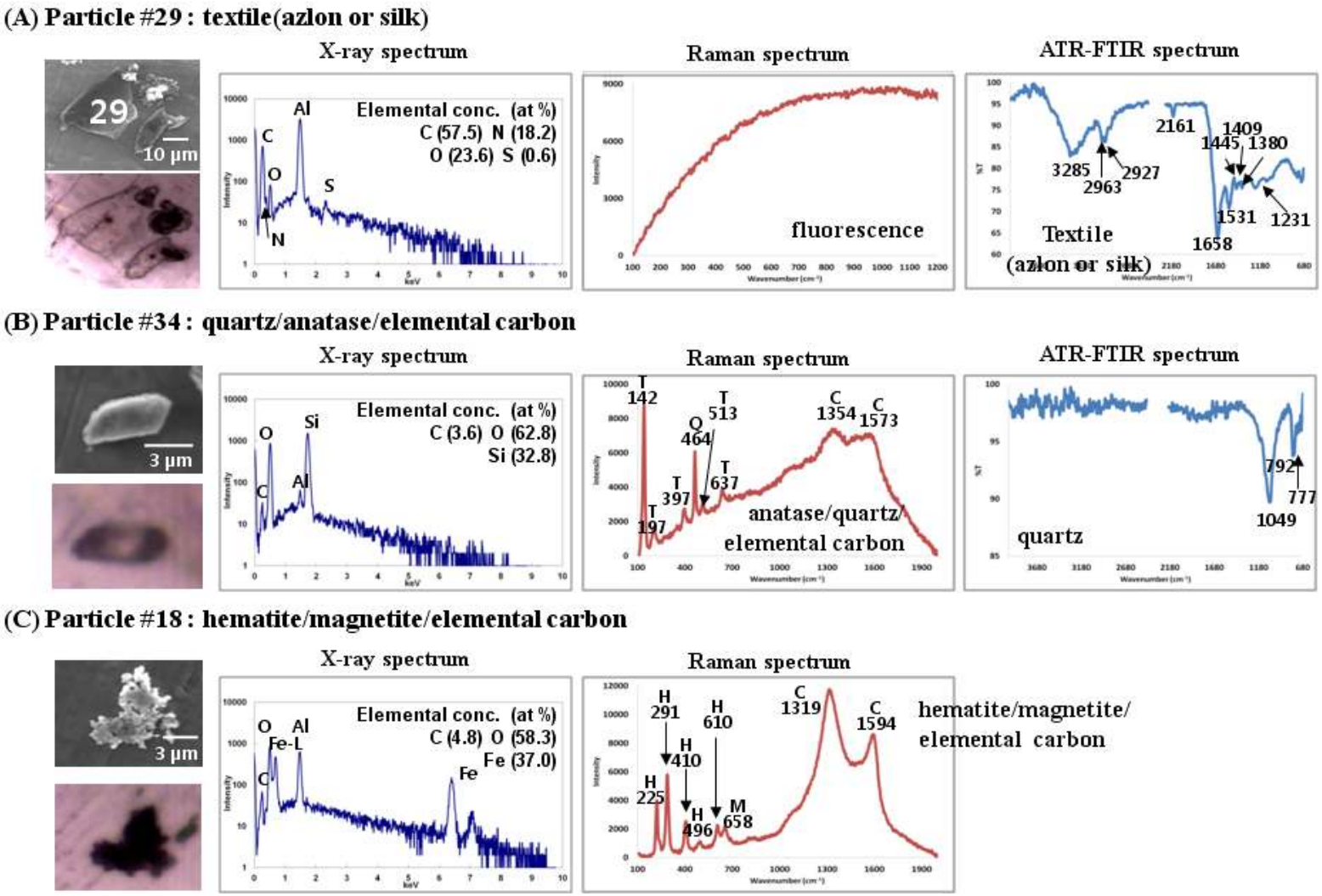

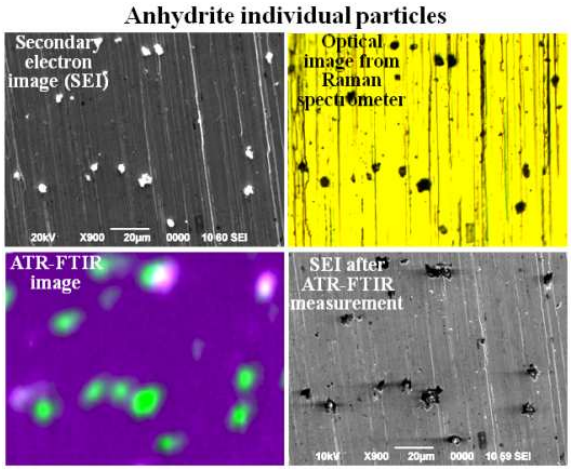

HIGHLIGHTS

- A quantitative ED-EPMA, RMS, and ATR-FTIR imaging techniques were used in combination for the analysis of the same individual particles for the first time.